

Research Article

Microscopic Investigation of Rate Dependence on Three-Point Notched-Tip Bending Sandstone

Wenshuai Li ^{1,2}, Faiz U. A. Shaikh ², Lianguo Wang ¹, Yinlong Lu ¹, Kai Wang ¹,
and Zhaolin Li ¹

¹State Key Laboratory for Geomechanics and Deep Underground Engineering, China University of Mining and Technology, Xuzhou, Jiangsu 221116, China

²Department of Civil Engineering, Curtin University, Perth, WA 6102, Australia

Correspondence should be addressed to Lianguo Wang; cumt_lgwang@163.com

Received 25 January 2019; Accepted 14 May 2019; Published 2 June 2019

Academic Editor: Andrea Spaggiari

Copyright © 2019 Wenshuai Li et al. This is an open access article distributed under the Creative Commons Attribution License, which permits unrestricted use, distribution, and reproduction in any medium, provided the original work is properly cited.

The cracking process in rock or concrete is usually characterized by the formation of microcracks that eventually form a propagating macrocrack. A series of three-point bending experiments were performed on sandstone containing Mode I crack under different loading rates. The microscopic monitoring system was established to capture the cracking process at notch tip. The loading rate dependence of microcracking behaviour was analysed based on load-time curves, acoustic emission (AE), microscopic images, and micrograph-based digital image correlation (DIC) technology. Results showed that the specimens underwent a short period of compression and elastic deformation stage under high loading rate, and the peak loads increased with the increase in loading rate. The AE results revealed that the fracturing process can be divided into elastic stage, damage stage, and postpeak stage, and more extensive damage occurred before the peak under low loading rate. It can be observed from microscopic images that the crack was initiated during the elastic stage, which was earlier than that determined from the AE monitoring. In addition, the microcracks were initiated at multiple locations and were mainly located at the interfaces between dense grains under low loading rate, while microcracks were observed inside the grains under high loading rate. Furthermore, the DIC results showed that the crack opening displacement (COD) of 0.6 mm/min at the peak was almost twice than that of 3.0 mm/min. The COD under the same loading rate at the peak can be considered as the material property of sandstone.

1. Introduction

With increase in demand for resources and energy, the relevant rock engineering activities, such as deep mining and development of geothermal resources, have increased [1–7]. The cracking process in quasibrittle materials such as rocks and concretes in geotechnical engineering is usually characterized by the formation of microcracks that eventually merge and form a propagating macrocrack. Previous studies have shown that, during the cracking process of rock, the local deformation and damage (microcracking) behaviour occurring in the microregion near the crack tip play a decisive role in controlling the macroscopic fracture behaviour [8]. Moreover, in deep mining, crack initiation and propagation due to the mining rate effect cause rib spalling, rock burst, and

other disasters [9–11]. Therefore, the research focusing on the cracking process of rock under different loading rates on a microscale is of great significance to better understand rock fracture behaviour and establish fracture mechanical model.

Previous studies have focused on the fracture behaviour of rock materials [12]. For example, Muralidhara et al. [13] and Ohno et al. [14] studied the fracture characteristics of concrete and determined the length of fracture process zone and initiation stress using acoustic emission (AE) location or energy. Based on AE locations and electronic speckle pattern interferometry images, Lin et al. [15] quantified the fracture characteristics in sandstone damage zones. For different loading rates, Backers et al. [16, 17] discussed the influence of loading rates on fracture toughness and surface roughness. Wang et al. [18] studied the anisotropic shale tensile failure

by performing the Brazilian splitting tests under different strain rates. Mahanta et al. [19] studied the strain rate sensitivity to rock fracture toughness, and the results indicated that, with increasing strain rates, the fracture toughness and tensile strength gradually increased. Previous studies have shown that the parameters of fracture velocity, rock strength, and fracture initiation toughness exhibited significant loading rate dependence [20–24]. However, the conventional monitoring methods, including AE and strain gauge, cannot supply adequate information about crack propagation, which restrict its application.

In recent years, digital image correlation (DIC) technology has been widely used to examine the fracture behaviour of quasibrittle materials [25–31]. Based on DIC technology, Lin and Labuz [32] defined the merged position of horizontal displacement contours as the fracture tip. Zhang et al. [33] described the fracture process of specimens using DIC, which was consistent with the AE results. Chen et al. [34] performed the three-point bending (TPB) tests to investigate the fracture parameters, such as crack opening displacement (COD). Due to low requirements for the measuring environment, simple realization, and complete deformation measurements, DIC technology provided a better way to examine crack propagation and rock fracture behaviour.

However, experimental investigations of mechanical properties and fracture behaviour of rocks were commonly performed at a macroscopic level [23]. In order to obtain the microcracking and microdeformation characteristics around the crack tip more accurately, combining a microscopic imaging platform with high spatial resolution with the DIC technique is an important trend to further develop rock fracture mechanical experiments [35–37]. Currently, the scanning electron microscope platforms have been used to conduct dynamic in situ detection under external loading [38]. Moreover, the DIC technology has been successfully applied across multiple length scales by generating a suitable speckle pattern at each scale [37, 39]. Nevertheless, due to harsh experimental conditions, there are many problems with the loading, testing, and specimen preparation for such experiments.

In this study, a series of TPB fracture experiments under different loading rates were conducted on sandstone containing a Mode I crack using a rigid electrohydraulic servocontrolled loading system. Moreover, a microscopic visualization monitoring system was established to observe the real-time in situ fracture characteristic of large-scale specimen at microscale. After that, quantitative measurements of microcracking and microdeformation behaviours in the microregion were achieved by micrograph-based DIC. Furthermore, the AE system was adopted to analyse the AE behaviour during the experiment. The loading rate dependence of microcracking and microdeformation behaviours was analysed and discussed.

2. Specimen Preparation and Experimental Setup

2.1. Specimen Preparation. The red sandstone was collected from Junan County, Linyi City, Shandong Province of

China. The sandstone belongs to the Wangshi and Qingshan groups of Mesozoic Cretaceous. Table 1 presents the detailed information about the tested sandstone. The sandstone was processed into a series of beam specimens with dimensions of 200 mm × 40 mm × 55 mm, as shown in Figure 1. All the specimens were fabricated from a large block of red sandstone. Meanwhile, the surfaces of specimens were polished using fine sand, and the nonparallelism and nonperpendicularity were both less than 0.02 mm. A thin saw blade was used to prefabricate a straight notch at the center of the bottom of the specimen (Mode I in Figure 1). The notch tip was smooth with the height and width of 15 mm and 1 mm, respectively (Figure 1(a)). A two-dimensional Cartesian coordinate system $o-xy$ was established for subsequent analysis and discussion. The origin of the coordinate system was located at the center of the prefabricated notch tip on the specimen surface, whereas the x -axis and y -axis represented the width and height directions of the notch, respectively (Figure 1(a)). The tested sandstone specimens are shown in Figure 1(b). Three tests were repeated for each loading rate to minimize the dispersion of test results caused by the heterogeneity of the sandstone specimen.

2.2. Experimental Method and Device. The TPB tests were performed under five constant loading rates of $v = 0.6$ mm/min (TPB-0.6), 1.0 mm/min (TPB-1.0), 1.4 mm/min (TPB-1.4), 1.8 mm/min (TPB-1.8), and 3.0 mm/min (TPB-3.0) using a rigid electrohydraulic servocontrolled loading system to investigate the effect of loading rate on fracture characteristics of the sandstone specimen. During the tests, the microscopic visualization monitoring system was arranged in front of the specimen (Figure 2(a)). Additionally, a DS2-8B AE monitoring system (Softland Times Scientific & Technology Co., Ltd, China; Figure 2(b)) was used to capture the AE activity inside the specimen during the loading process. The system consisted of AE host, AE sensors, and preamplifiers. The AE sensor had a diameter of 8 mm, and its monitoring frequency range was 100–900 kHz. The AE signals were amplified with the gain of 40 dB in a preamplifier, and the AE preamplifier had the advantages of low noise, wide bandwidth, impact resistance, and small volume. The time parameters for AE waveforms included peak definition time, hit definition time, and hit locking time and were set to be 50, 100, and 100 μ s, respectively. In addition, the threshold was set to be 10 mV to avoid the possibility of electronic or environmental noise [40]. A total of two AE sensors arranged around the specimen were directly in contact with the surface of the specimen (Figure 2(a)).

The microscopic visualization monitoring system was composed of a long working distance microscope, a high-speed camera, an image acquisition and control system, a precision electric mobile control platform, a shock absorbing ground support, and a lighting source, as shown in Figure 2(c). All of the experimental equipment were placed on a shock absorbing ground support to minimize the influence of environmental vibrations on the image acquisition process. The detailed information of the

TABLE 1: Detailed information of the tested sandstone.

Properties	Parameters
Main mineral components	41.0% feldspar
	34.8% debris
	12.6% quartz
	11.6% agglutinate
Initial porosity	7.3 (± 1.1)%
Grain size (mm)	0.1~0.35, medium-grained
Average density (kg/m ³)	2380

microscopic visualization monitoring system can be found by Lu et al. [40].

2.3. DIC Analysis. DIC has the advantages of noncontact measurements and high precision and has been widely used to detect the fracture behaviour of rock and concrete. In this study, a series of micrographs were acquired using the microscopic visualization monitoring system. Then, the DIC technique was applied to accurately analyse the microscopic deformation behaviour in local microregions at notch tip during the loading process. In the DIC calculations, the deformation field in local microregions can be obtained by matching the measurement points of the images before (reference image) and after the deformation (target image) [35, 41], as illustrated in Figure 3.

A square reference subset of $(2N+1) \times (2N+1)$ pixels, centered at point $P(x, y)$, is selected from the reference image. Then, a searching subset ($M > N$) with the size of $(2M+1) \times (2M+1)$ pixels is chosen from the target image (Figure 3). Assume that the point P in the reference image with an x - and y -coordinate system is mapped into point P' in the deformed image, the point $P'(x, y)$ can be defined using the following equation:

$$\begin{cases} x' = x + u + \frac{\partial u}{\partial x} \Delta x + \frac{\partial u}{\partial y} \Delta y, \\ y' = y + v + \frac{\partial v}{\partial x} \Delta x + \frac{\partial v}{\partial y} \Delta y, \end{cases} \quad (1)$$

where u and v are the displacement components of the subset center point in x and y directions, respectively. Furthermore, Δx and Δy are the distances from point P to subset center point, while $\partial u/\partial x$, $\partial u/\partial y$, $\partial v/\partial x$, and $\partial v/\partial y$ are the gradients of displacement components for the subset.

The correlation calculation is conducted between the reference subset and each searching subset based on a predefined correlation function. The subset with the maximum correlation coefficient is identified as the location of the target subset. The central point $P'(x, y)$ of the target subset (after deformation) can be regarded as the same point as the point P to be measured (before deformation). The zero-mean normalized sum of squared differences correlation criterion is used to evaluate the degree of similarity between the reference subset and the searching subset [41]:

$$C_{\text{ZNSSD}} = \sum_{x=1}^{2N+1} \sum_{y=1}^{2N+1} \left(\frac{f(x, y) - f_m}{\sqrt{\sum_{x=1}^{2N+1} \sum_{y=1}^{2N+1} [f(x, y) - f_m]^2}} - \frac{g(x', y') - g_m}{\sqrt{\sum_{x=1}^{2N+1} \sum_{y=1}^{2N+1} [g(x', y') - g_m]^2}} \right)^2, \quad (2)$$

where $f(x, y)$ is the pixel gray value at coordinates (x, y) in the reference subset of the reference image and $g(x', y')$ is the pixel gray value at coordinates (x', y') in the searching subset of the target image. Furthermore, f_m and g_m are the mean intensity values of the reference and target subsets, respectively.

3. Results and Discussion

3.1. Load-Time Curve. Figure 4 shows the typical load-time (P - t) curves for TPB tests on specimens under different loading rates (0.6, 1.0, 1.4, 1.8, and 3.0 mm/min). The results showed that the P - t curve under different loading rates increased with time, and after reaching the peak value, it decreased with time, leading to strain softening. For TPB-0.6-1, the specimen underwent a long period of compression and elastic deformation. At a high loading rate, the specimen reached the peak load in a relatively short time. The average peak loads under different loading rates are shown in Figure 5. As the loading rate increased, the peak load increased as well.

3.2. AE Behaviour. AE can be used to monitor crack initiation and propagation in rock specimens [42]. Figure 6 shows the typical load-time (P - t) curves together with AE count rate for the loading rates of 0.6, 1.0, 1.4, 1.8, and 3.0 mm/min. During the loading process, AE characteristics for specimens under different loading rates exhibited similar behaviour, which can be divided into three stages, including elastic stage (Stage I), damage stage (Stage II), and postpeak stage (Stage III) (Figure 6). Amongst these, Stage II began at the load, at which the AE signal increased significantly for the first time [43, 44].

For specimen TPB-0.6-1 (Figure 6(a)), during Stage I, there were almost no AE events, which indicated that no fracturing occurred (Figure 6(a)). When the specimen was loaded to 79.4% of the P_{peak} (Stage II), the AE count rate increased significantly and the microcrack began to appear. During Stage III, the AE events continued to increase rapidly, and the AE activity became significantly intense. The macrocracks appeared during this stage and led to failure of specimens. However, under high loading rate, few AE events occurred before the peak (Figures 6(b)–6(e)), whereas during Stage II, the number of AE events decreased significantly (Figure 6(e)). The results clearly showed that the loading rate significantly affected the damage process.

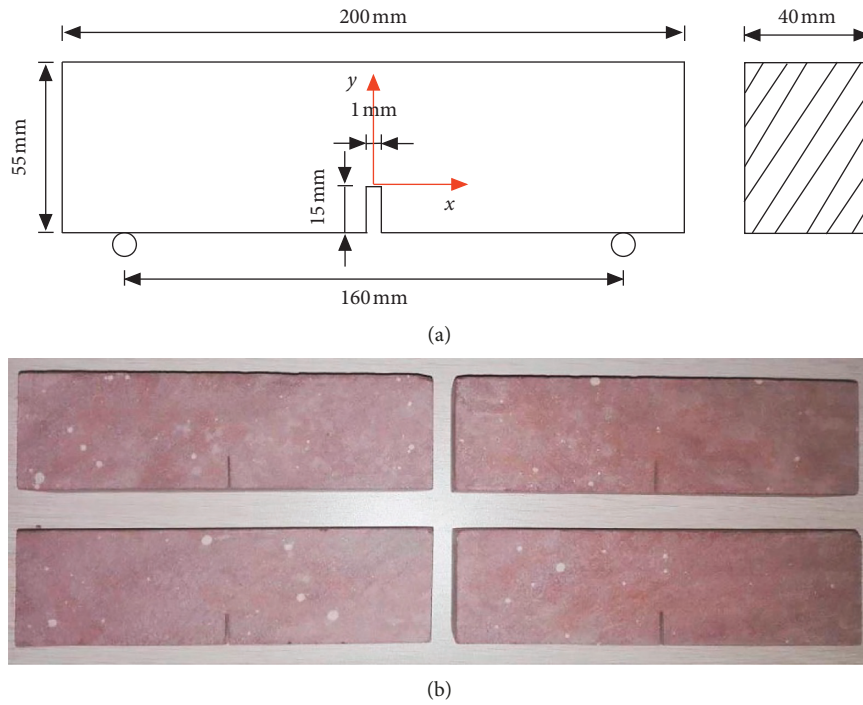


FIGURE 1: Preparation of the sandstone specimens for the TPB experiments: (a) schematic of the specimen and (b) the tested sandstone specimens.

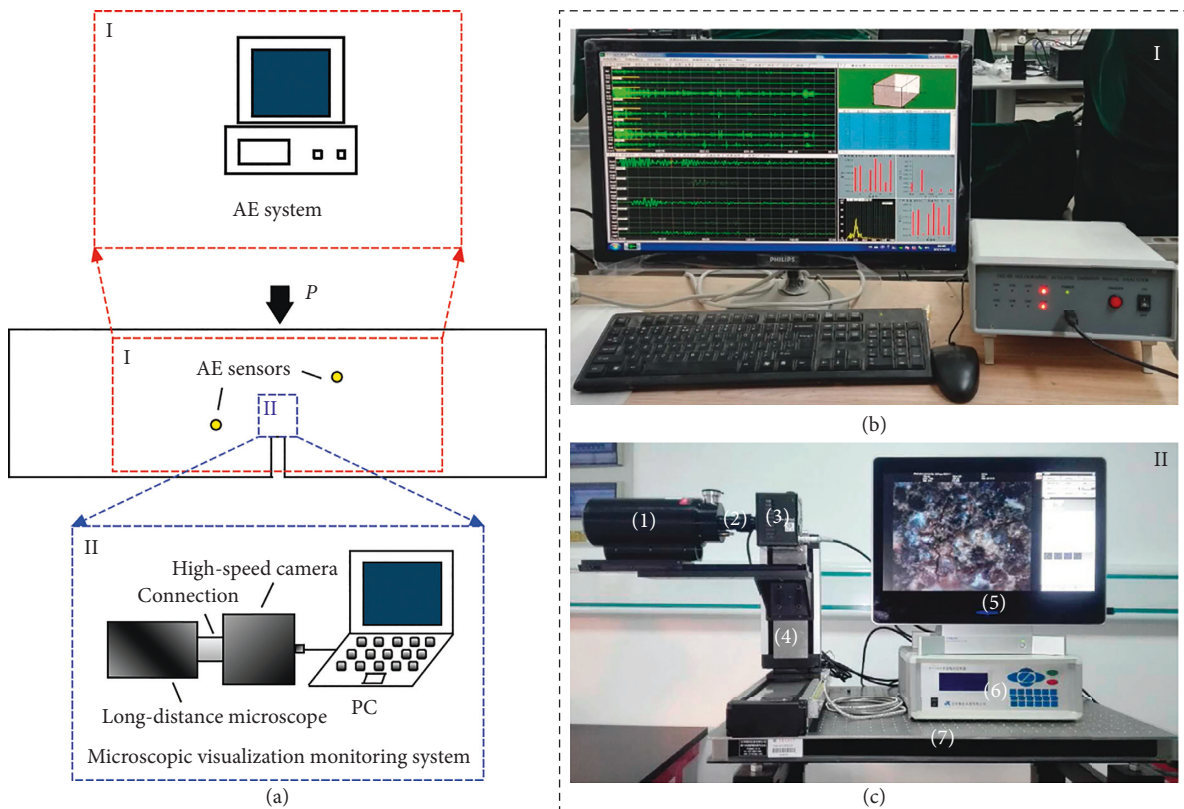


FIGURE 2: Real-time in situ cracking microscopic visualization monitoring system: (a) schematic of the test system, (b) AE monitoring system, and (c) microscopic visualization monitoring system. Note: (1) long working distance microscope, (2) C-mount interface, (3) high-speed video camera, (4) precision electric mobile platform, (5) image acquisition and control system, (6) stepping motor controller, and (7) shock absorbing ground support.

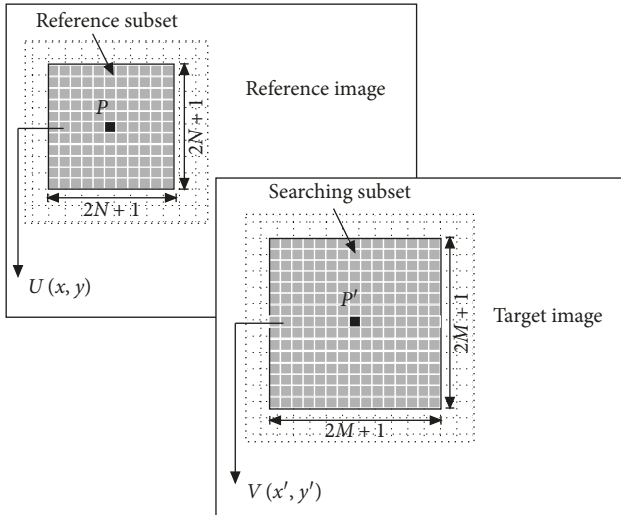


FIGURE 3: Schematic of the DIC calculation.

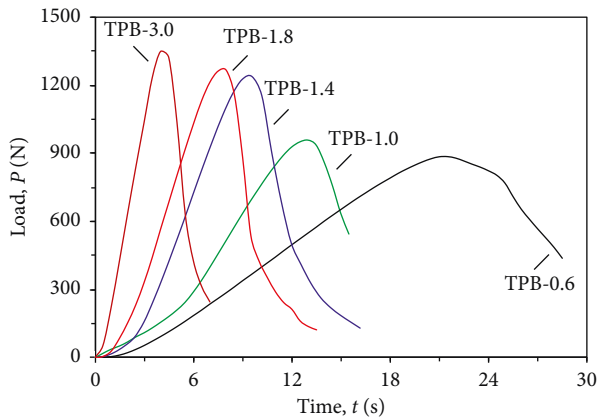


FIGURE 4: Typical load-time curves for the TPB tests on sandstone specimens under different loading rates.

3.3. Crack Initiation and Propagation. In order to visually identify the microscopic fracture characteristics during the loading process under different loading rates, the images of the cracking process captured using the microscopic visualization monitoring system were analysed. Figure 7 shows the typical microscopic cracking process under the loading rates of 0.6 mm/min (Figure 7(a)) and 3.0 mm/min (Figure 7(b)). In the figure, the field of view of $0.8 \text{ mm} \times 1.0 \text{ mm}$ around the notch tip was selected.

For specimen TPB-0.6-1, it can be observed that, when the specimen was loaded to 70% of P_{peak} (Point A in Figure 7(a)), a new crack initiated above the notch tip. This observation implied that the crack initiation load, as determined by the captured microscopic image, was smaller than that determined from the AE results, which was 79.4% of the P_{peak} (Point B in Figure 6(a)). Further analysis of the captured microscopic images showed that the microcracks were initiated at multiple locations at the notch tip (Point C in Figure 7(a)). At the peak, a total of three cracks (Crack 1, Crack 2, and Crack 3) appeared in the field of view (Point D in Figure 7(a)). When the load increased to the postpeak

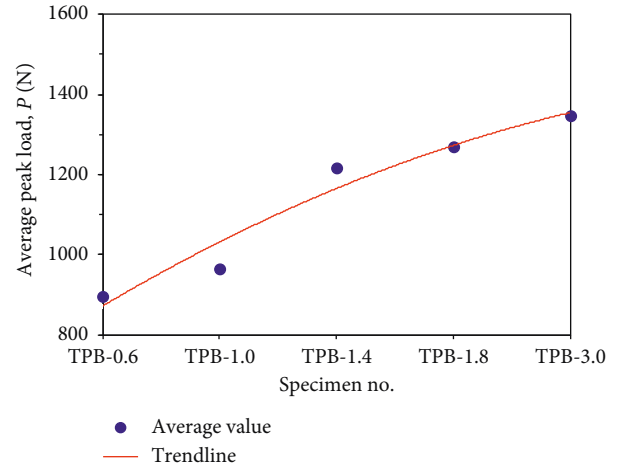


FIGURE 5: Average peak loads for the TPB tests on sandstone specimens under different loading rates.

stage, Crack 3 opened further, whereas Crack 2 was closed (Point E in Figure 7(a)). These new cracks gradually propagated and coalesced into one main crack (Point F in Figure 7(a)). The main crack propagated further upwards in a zigzag and irregular way, approximately along the loading direction until the specimen failed. It was clear that the propagation of microcracks was not instantaneous, but rather gradual along the regions of weak strength. As revealed by microscopic images in Figure 7(a), specimen failure results of gradual localized deformation took place in the grain boundary of the microstructure (Crack 1 in Point B, Crack 2 in Point C, and Crack 3 in Point D). It can be considered that the stress did not reach the grain strength.

For comparison, Figure 7(b) shows the microscopic cracking process under the loading rate of 3.0 mm/min. Clearly, the crack was observed at 84% of P_{peak} , which was earlier than that determined from the AE results 92.5% of P_{peak} (Point D in Figure 6(e)). At the peak, three cracks appeared in the field of view (Crack 1, Crack 2, and Crack 3; Point E in Figure 7(b)). The three cracks at the peak were narrower than those under the loading rate of 0.6 mm/min (Point D in Figure 7(a)). After the peak, the three cracks gradually propagated and connected with each other (Point G in Figure 7(b)). Compared with the specimen TPB-0.6-1, a microcrack was observed inside the grain in the specimen TPB-3.0-1 (Crack 3; Point E in Figure 7(b)). This was due to the reason that microcracks did not have sufficient time to propagate and were forced to propagate along a shorter path with higher resistance under a high loading rate [45, 46].

Furthermore, Figure 8 shows the typical surface microscopic images at the peak under different loading rates, as observed using the microscopic visualization monitoring system. In this case, the microscopic crack morphologies at the peak under five different loading rates were both irregular. For specimen TPB-0.6-1, the microcracks were formed at multiple locations at the notch tip with a certain width. When the loading rates increased, narrower cracks at the peak were observed. This was because the microcracks did not have sufficient time to fully propagate under a high

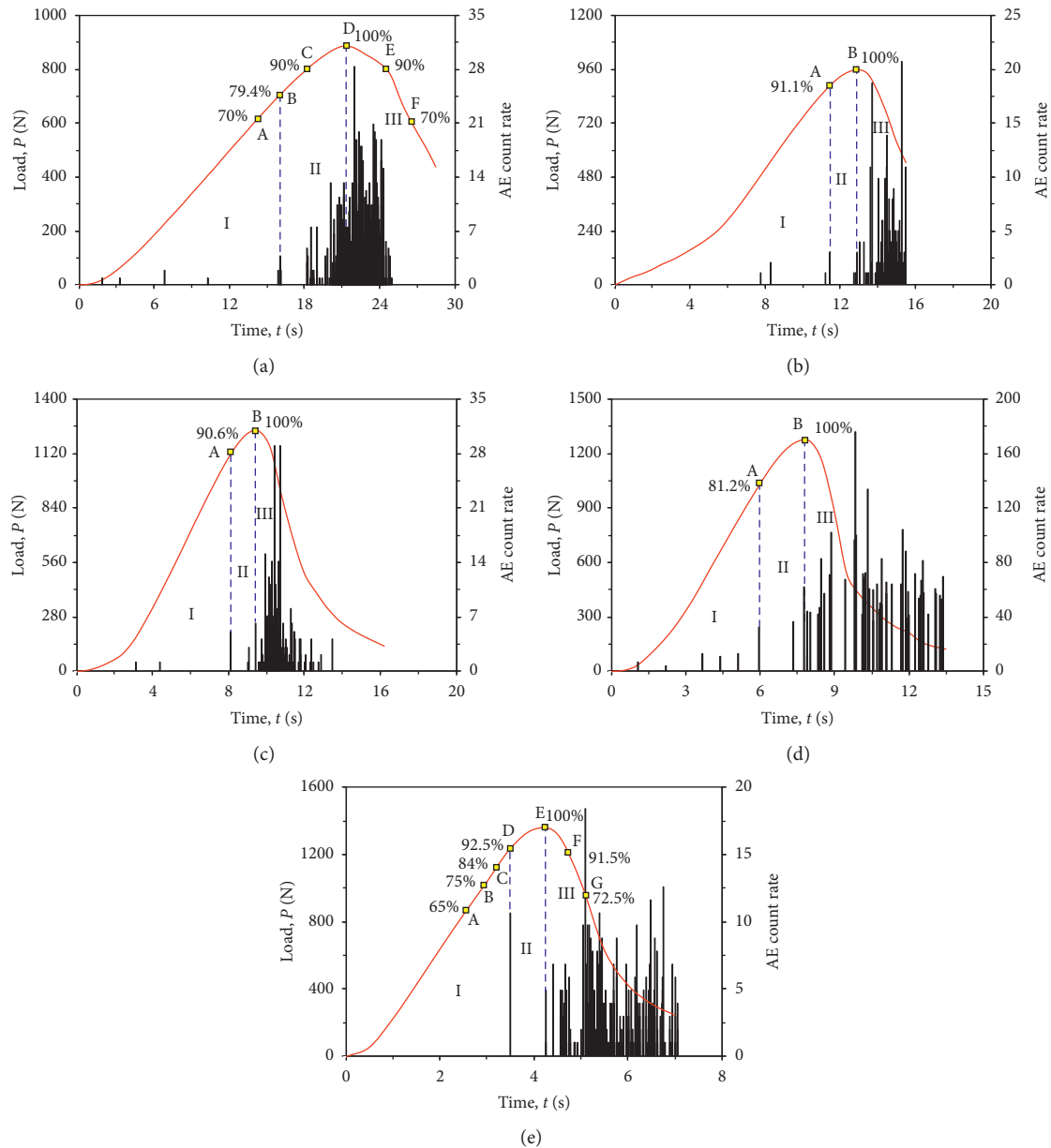


FIGURE 6: Typical variation in load and AE count rate with time for TPB tests under different loading rates: (a) 0.6 mm/min, (b) 1.0 mm/min, (c) 1.4 mm/min, (d) 1.8 mm/min, and (e) 3.0 mm/min. I, II, and III represent elastic stage, damage stage, and postpeak stage, respectively.

loading rate, which was accompanied by few AE events before peak (Figure 6). The crack opening width under different loading rates will be quantitatively discussed in Section 3.4. Moreover, it can be observed that these localized microcracks were mainly located at the interfaces between dense grains, especially for low loading rate, whose tortuous propagation was conditioned by the arrangement of grains or weak zones.

Table 2 summarizes the crack initiation load ratios of the tested specimens with different loading rates, as obtained from the AE monitoring and the microscopic images. The results showed that the crack initiation loads, determined from the captured microscopic images using the microscopic visualization monitoring system, were smaller than

those determined from the AE results. This observation indicated that the microscopic visualization monitoring system can capture more crack initiation information than the AE. Furthermore, the crack initiation load ratio at the peak observed using the microscopic images increased dramatically from the loading rate of 0.6 mm/min to 3.0 mm/min. Compared with the specimen of TPB-0.6, the average value of the crack initiation load ratio with the loading rates of 1.0, 1.4, 1.8, and 3.0 mm/min was increased by ~ 2.0 , 4.1, 8.8, and 10.1%, respectively. This result can be explained based upon the microscopic damage mechanism. Under the low loading rate, the microcracks were fully propagated, leading to a low initiation load and more AE events before peak (Figure 6(a)). However, under a high

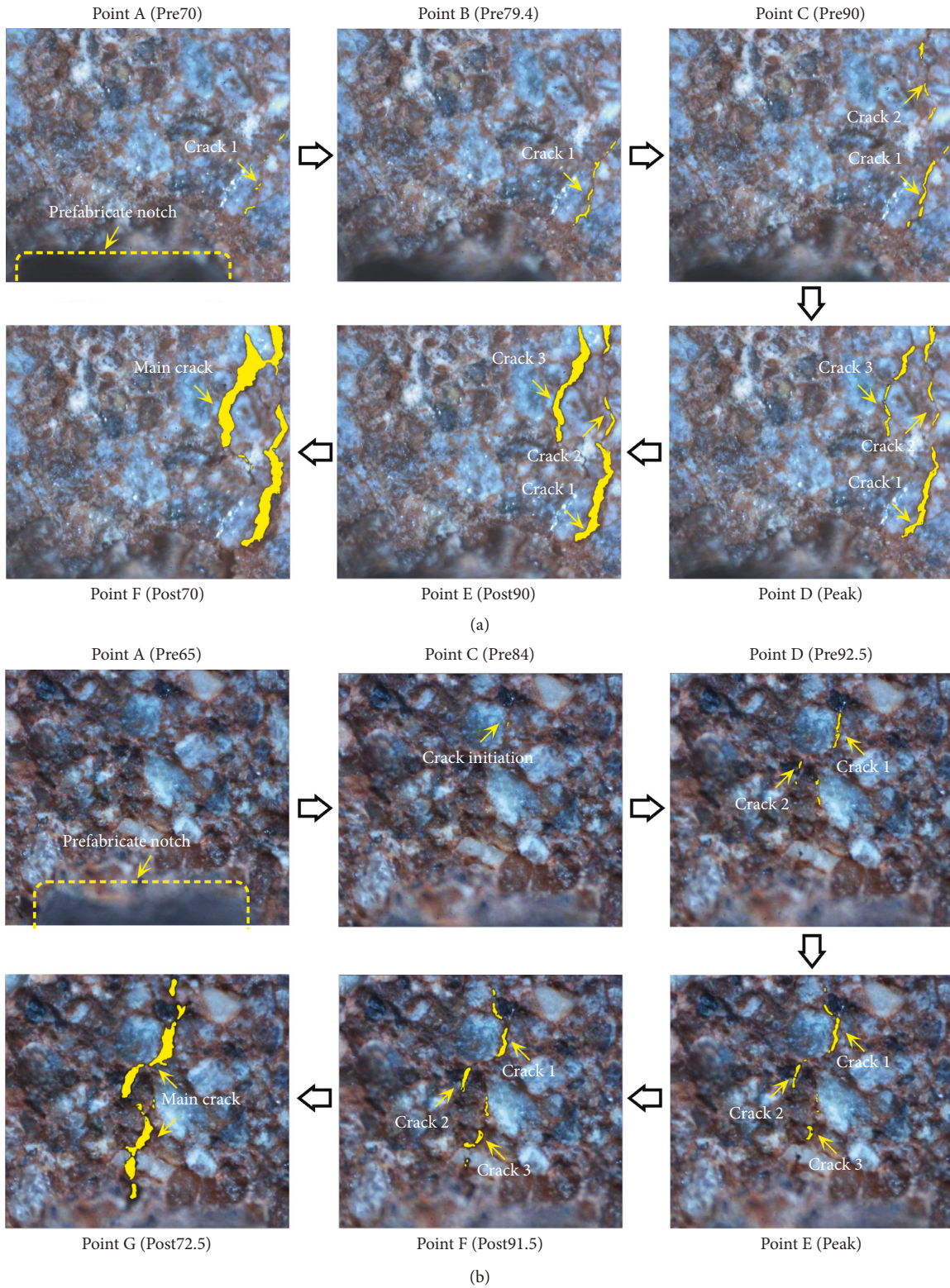


FIGURE 7: Microscopic cracking process with the field of view of 0.8 mm × 1.0 mm around notch tip under the typical loading rates of (a) 0.6 mm/min (TPB-0.6-1) and (b) 3.0 mm/min (TPB-3.0-1) observed using the microscopic visualization monitoring system. “Pre70” denotes the 70% of P_{peak} prior to the peak, while “Post90” denotes the 90% of P_{peak} after the peak.

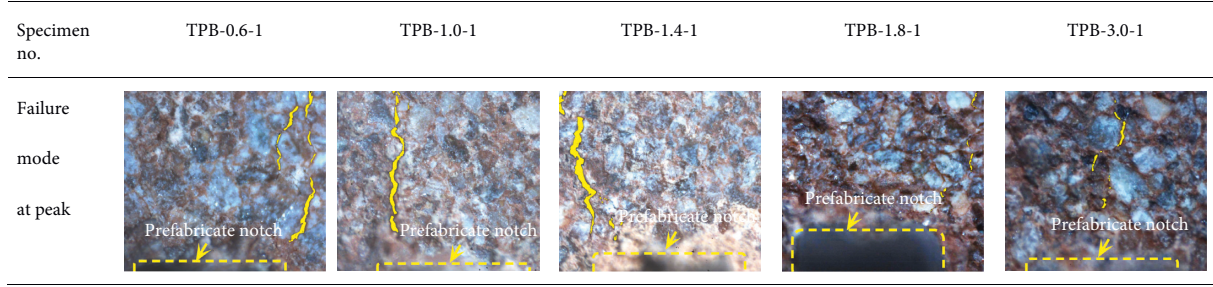


FIGURE 8: Typical microscopic failure modes at the peak for five loading rates, as observed using the microscopic visualization monitoring system.

TABLE 2: Crack initiation loads of specimens with different loading rates obtained from AE results and microscopic visualization monitoring system.

Specimen no.	AE monitoring		Microscopic monitoring	
	Experiment (%)	Average (%)	Experiment (%)	Average (%)
TPB-0.6-1	79.4		64.2	
TPB-0.6-2	76.3	79.3	70.5	71.3
TPB-0.6-3	82.3		79.1	
TPB-1.0-1	91.1		69.3	
TPB-1.0-2	87.5	88.0	75.1	72.7
TPB-1.0-3	85.4		73.6	
TPB-1.4-1	90.6		74.8	
TPB-1.4-2	88.8	90.4	71.6	74.2
TPB-1.4-3	91.8		76.2	
TPB-1.8-1	85.2		81.2	
TPB-1.8-2	89.9	90.0	76.4	77.6
TPB-1.8-3	91.8		75.3	
TPB-3.0-1	92.5		79.8	
TPB-3.0-2	93.2	92.1	80.6	78.5
TPB-3.0-3	90.5		75.2	

loading rate, the microcracks did not have sufficient time to propagate, which brought about a high crack initiation load and few AE events.

3.4. Deformation Characteristics at Notch Tip. Based on the captured microscopic images of specimens, the DIC technique was applied to quantitatively calculate the displacement fields at the notch tip. Figure 9 shows the distributions of horizontal incremental displacement at the notch tip for specimen TPB-0.6-1 under different loading levels. A range of 0.8 mm \times 1.0 mm ahead of the notch was selected for DIC calculation, as shown in Figure 9. The incremental displacement was calculated based on the comparison of two selected images at different loading levels (i.e., the reference and the target images). For example, “Pre70-Pre79.4” in Figure 9 indicated that the images captured at 70% P_{peak} and 79.4% P_{peak} were selected as the reference image and the target image for DIC calculation, respectively. It should be noted that the DIC algorithm involved larger computational errors if the displacement increment was large. To avoid computational errors resulting from excessive micro-deformation, the horizontal incremental displacement was evaluated under a short loading level, such as “Pre70-Pre79.4” or “Pre90-Pre95” in Figure 9, instead of “Pre70-

Pre95.” In addition, Figure 10 presents the total horizontal incremental displacement for specimen TPB-0.6-1 at the notch tip under different loading levels ($y = 0$ mm above the notch tip). Of course, the total displacements can be obtained by summing all the incremental displacements, as shown in Figure 10.

It can be seen from Figure 9 that the discontinuous deformation zone at multiple locations at the notch tip was clearly observed during the late elastic stage (“Pre70-Pre79.4” in Figure 9). The contours merged on the side of the notch, at $x = 0$, $y = 0-0.5$ mm. During the initial stage of damage, the discontinuous deformation zone coalescence was detected in the DIC calculation region (“Pre85-Pre90” and “Pre90-Pre95” in Figure 9). When the specimen was loaded to 90% P_{peak} , a horizontal displacement jump (Figure 10) appeared at the notch tip, which was due to the opening of induced cracking. The crack opening width was 13.85 μm (the horizontal displacement changes from approximately $-9.31 \mu\text{m}$ to 4.54 μm in Figure 10). As the load increased to peak, the displacement discontinuous zone founded by “Pre95-Pre98” and “Pre98-Peak” did not follow the observation obtained from “Pre85-Pre90” and “Pre90-Pre95” (Figure 9). This can be explained that the DIC calculation results reflected the change between the two loading levels. At the peak, the displacement had a larger magnitude

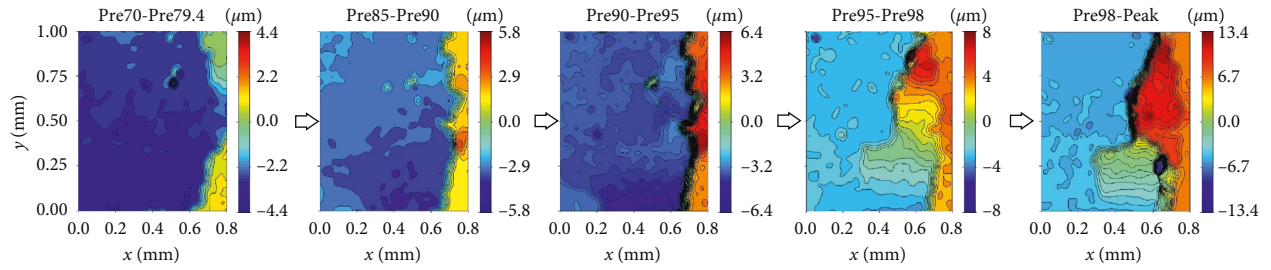


FIGURE 9: Distributions of horizontal incremental displacement at notch tip for specimen TPB-0.6-1 with the range of $0.8 \text{ mm} \times 1.0 \text{ mm}$ based on the DIC calculation obtained from the microscopic images under different loading levels.

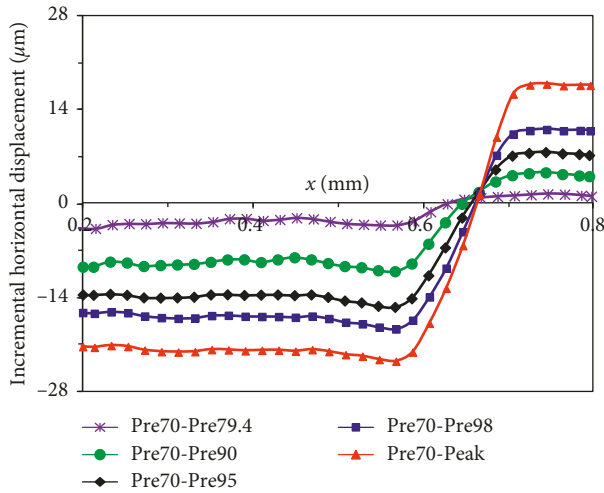


FIGURE 10: Variation in total horizontal incremental displacement for specimen TPB-0.6-1 along the line $y = 0 \text{ mm}$ in Figure 9 under different loading levels.

of jump and ranged from $-23.15 \mu\text{m}$ to $17.51 \mu\text{m}$ (a jump magnitude of $40.66 \mu\text{m}$). The discontinuous deformation zone obtained from the DIC results was consistent with the microscopic crack morphology (Figure 7(a)).

By contrast, Figure 11 plots the distributions of horizontal incremental displacement at the notch tip for specimen TPB-3.0-1 under different loading levels. For DIC calculations, a range of $0.6 \text{ mm} \times 0.9 \text{ mm}$ ahead of the notch was selected, as shown in Figure 11. Figure 12 shows the variations in horizontal incremental displacement for specimen TPB-3.0-1 at the notch tip under different loading levels ($y = 0 \text{ mm}$ above the notch tip). In the elastic stage, the deformation discontinuous zone was observed (“Pre65-Pre75” and “Pre65-Pre84” in Figure 11). A horizontal displacement jump, from approximately $-4.16 \mu\text{m}$ to $3.60 \mu\text{m}$, as shown in Figure 12 (“Pre65-Pre84”), was detected at the notch tip. The displacement jump zone was 0.16 mm between $x = -0.08 \text{ mm}$ and $x = 0.08 \text{ mm}$. As the test progressed to the peak, the horizontal displacement changed from $-11.60 \mu\text{m}$ to $11.42 \mu\text{m}$ (crack opening width of $23.02 \mu\text{m}$), while the displacement jump zone ranged from $x = -0.07 \text{ mm}$ to $x = 0.08 \text{ mm}$ (a jump zone of 0.15 mm). The discontinuous deformation zone and the displacement jump range were both narrow enough. This indicated that the macroscopic cracks had begun to form.

Figure 13 shows the total incremental CODs at the peak under five loading rates determined from the micrograph-based DIC. In the figure, the total CODs above the notch tip ($y = 0 \text{ mm}$) were calculated by summing all the incremental opening displacements from crack initiation to peak. Clearly, the CODs under the same loading rate at the peak were nearly equal, which can be considered as the material property of sandstone. Moreover, the COD under the low loading rate was larger than that of the high loading rate. Compared with the specimen at the loading rate of 0.6 mm/min , the average value of COD at the peak with the loading rates of 1.0 , 1.4 , 1.8 , and 3.0 mm/min was declined by ~ 1.8 , 2.9 , 20.5 , and 44.6% , respectively. This can be attributed to the fact that a high loading rate delayed both the microcracking localization and macrocrack propagation, leading to a decrease in the COD at the peak load.

4. Conclusions

In this study, TPB fracture experiments on sandstone containing a Mode I crack were conducted using a rigid electrohydraulic servocontrolled loading system along with the microscopic visualization monitoring system and AE monitoring. The evolution of cracking process at notch tip and loading rate dependence of sandstone microcracking and microdeformation behaviour were analysed and discussed. The following conclusions can be drawn.

The peak loads increased with the increase in the loading rate. The sandstone specimens underwent a short period of compression and elastic deformation stage under high loading rate. The microcracks did not have sufficient time to propagate and were forced to propagate along a short path with higher resistance under high loading rate.

The AE monitoring results revealed that the fracturing process can be divided into three stages: elastic stage, damage stage, and postpeak stage. More extensive damage occurred before the peak load under low loading rate, indicating that microcracks could fully propagate, leading to a low crack initiation load.

The evolution of the cracking process during the whole loading process of specimens was captured using the real-time microscopic visualization monitoring system under different loading rates. The microscopic images revealed that the crack initiated during Stage I, which was earlier than that determined from the AE monitoring. The microcracks initiated at multiple locations at the notch tip and gradually

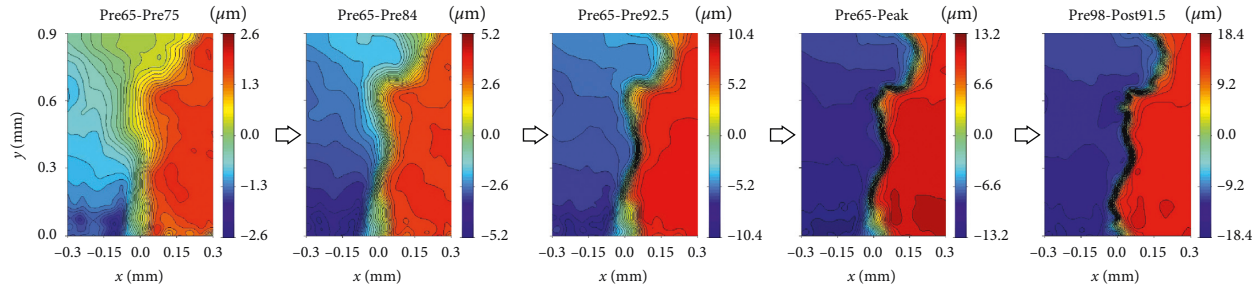


FIGURE 11: Distributions of horizontal incremental displacement at notch tip for specimen TPB-3.0-1 with the range of $0.6 \text{ mm} \times 0.9 \text{ mm}$ based on the DIC calculation obtained from the microscopic images under different loading levels.

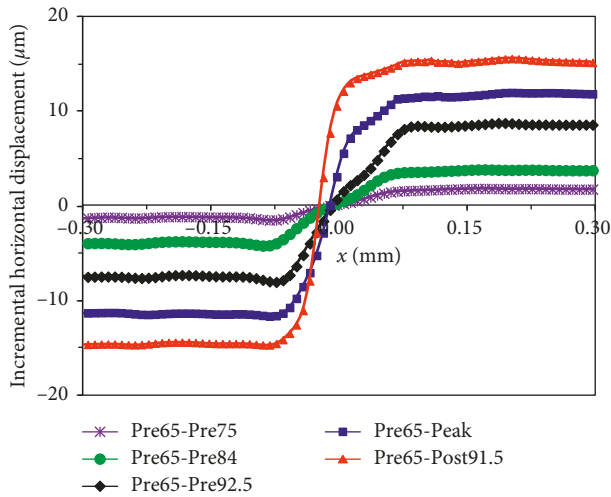


FIGURE 12: Variation in total horizontal incremental displacement for specimen TPB-3.0-1 along the line $y = 0 \text{ mm}$ in Figure 11 under different loading levels.

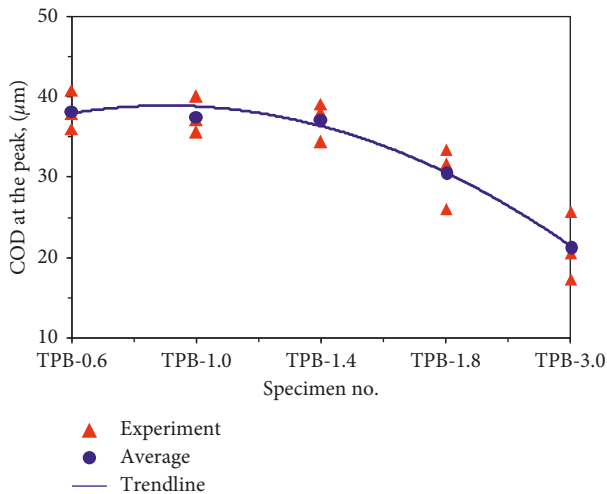


FIGURE 13: The total incremental CODs at the peak under five loading rates determined by DIC.

propagated and coalesced into one main crack. These localized microcracks were mainly located at the interfaces between dense grains, especially for low loading rate, whose tortuous propagation was conditioned by the arrangement

of grains or weak zones. However, the microcrack was observed inside the grain under high loading rate.

The displacement fields at the notch tip were quantitatively calculated using DIC technology at different loading rates. This procedure was based on the comparison of images acquired at different loading levels and provides quantitative descriptions of local responses. The results showed that the discontinuous deformation zone at multiple locations at the notch tip was clearly observed during the late elastic stage, which allowed the evaluation of the impact of material heterogeneity on the strain distribution and localization. As the load increased, the displacement jump range was narrow enough, which was consistent with the real microscopic crack morphology results. The CODs under the same loading rate at the peak can be considered as the material property of sandstone. The average COD at the peak under low loading rate (TPB-0.6) was almost twice than that of high loading rate (TPB-3.0).

Data Availability

The data used to support the findings of this study are available from the corresponding author upon request.

Conflicts of Interest

The authors declare that they have no conflicts of interest.

Acknowledgments

The authors gratefully acknowledge the support of joint Ph.D program of “double first rate” construction disciplines of CUMT.

References

- [1] H. P. Xie, Y. Ju, F. Gao, M. Z. Gao, and R. Zhang, “Groundbreaking theoretical and technical conceptualization of fluidized mining of deep underground solid mineral resources,” *Tunnelling and Underground Space Technology*, vol. 67, pp. 68–70, 2017.
- [2] M. A. Perras, H. Wannenmacher, and M. S. Diederichs, “Underground excavation behaviour of the queenston formation: tunnel back analysis for application to shaft damage dimension prediction,” *Rock Mechanics and Rock Engineering*, vol. 48, no. 4, pp. 1647–1671, 2015.

- [3] L. Charlet, P. Alt-Epping, P. Wersin, and B. Gilbert, "Diffusive transport and reaction in clay rocks: a storage (nuclear waste, CO₂, H₂), energy (shale gas) and water quality issue," *Advances in Water Resources*, vol. 106, pp. 39–59, 2017.
- [4] S. M. Chen, A. X. Wu, Y. M. Wang, X. Chen, R. F. Yan, and H. J. Ma, "Study on repair control technology of soft surrounding rock roadway and its application," *Engineering Failure Analysis*, vol. 92, pp. 443–455, 2018.
- [5] Y. L. Tan, F. H. Yu, J. G. Ning, and T. B. Zhao, "Design and construction of entry retaining wall along a gob side under hard roof stratum," *International Journal of Rock Mechanics and Mining Sciences*, vol. 77, no. 77, pp. 115–121, 2015.
- [6] B. Y. Jiang, S. T. Gu, L. G. Wang, G. C. Zhang, and W. S. Li, "Strainburst process of marble in tunnel-excavation-induced stress path considering intermediate principal stress," *Journal of Central South University*, vol. 26, no. 4, pp. 984–999, 2019.
- [7] M. Chen, S. Q. Yang, R. Pathegama Gamage et al., "Fracture processes of rock-like specimens containing nonpersistent fissures under uniaxial compression," *Energies*, vol. 12, no. 1, p. 79, 2019.
- [8] J. R. Yates, M. Zanganeh, and Y. H. Tai, "Quantifying crack tip displacement fields with DIC," *Engineering Fracture Mechanics*, vol. 77, no. 11, pp. 2063–2076, 2010.
- [9] B. Y. Jiang, L. G. Wang, Y. L. Lu, C. Q. Wang, and D. Ma, "Combined early warning method for rockburst in a Deep Island, fully mechanized caving face," *Arabian Journal of Geosciences*, vol. 9, no. 20, p. 743, 2016.
- [10] S. T. Gu, B. Y. Jiang, G. S. Wang, H. B. Dai, and M. P. Zhang, "Occurrence mechanism of roof-fall accidents in large-section coal seam roadways and related support design for Bayangaole coal mine, China," *Advances in Civil Engineering*, vol. 2018, Article ID 6831731, 17 pages, 2018.
- [11] Y. L. Tan, X. S. Liu, J. G. Ning, and Y. W. Lu, "In situ investigations on failure evolution of overlying strata induced by mining multiple coal seams," *Geotechnical Testing Journal*, vol. 40, no. 2, pp. 244–257, 2017.
- [12] X. Wang, Z. J. Wen, Y. J. Jiang, and H. Huang, "Experimental study on mechanical and acoustic emission characteristics of rock-like material under non-uniformly distributed loads," *Rock Mechanics and Rock Engineering*, vol. 51, no. 3, pp. 729–745, 2018.
- [13] S. Muralidhara, B. K. R. Prasad, H. Eskandari, and B. L. Karihaloo, "Fracture process zone size and true fracture energy of concrete using acoustic emission," *Construction and Building Materials*, vol. 24, no. 4, pp. 479–486, 2010.
- [14] K. Ohno, K. Uji, A. Ueno, and M. Ohtsu, "Fracture process zone in notched concrete beam under three-point bending by acoustic emission," *Construction and Building Materials*, vol. 67, no. 6, pp. 139–145, 2014.
- [15] Q. Lin, A. Fakhimi, M. Haggerty, and J. F. Labuz, "Initiation of tensile and mixed-mode fracture in sandstone," *International Journal of Rock Mechanics and Mining Sciences*, vol. 46, no. 3, pp. 489–497, 2009.
- [16] T. Backers, N. Fardin, G. Dresen, and O. Stephansson, "Effect of loading rate on Mode I fracture toughness, roughness and micromechanics of sandstone," *International Journal of Rock Mechanics and Mining Sciences*, vol. 40, no. 3, pp. 425–433, 2003.
- [17] T. Backers, S. Stanchits, and G. Dresen, "Tensile fracture propagation and acoustic emission activity in sandstone: the effect of loading rate," *International Journal of Rock Mechanics and Mining Sciences*, vol. 42, no. 7–8, pp. 1094–1101, 2005.
- [18] Y. Wang, C. H. Li, Y. Z. Hu, and T. Q. Mao, "Brazilian test for tensile failure of anisotropic shale under different strain rates at quasi-static loading," *Energies*, vol. 10, no. 9, p. 1324, 2017.
- [19] B. Mahanta, N. Sirdesai, T. N. Singh, and P. G. Ranjith, "Experimental study of strain rate sensitivity to fracture toughness of rock using flattened Brazilian disc," *Procedia Engineering*, vol. 191, pp. 256–262, 2017.
- [20] F. Yan, X. T. Feng, K. Xia, and C. Jin, "Dynamic tensile failure of the rock interface between tuff and basalt," *Rock Mechanics and Rock Engineering*, vol. 45, no. 3, pp. 341–348, 2012.
- [21] H. C. Sang, Y. Ogata, and K. Kaneko, "Strain-rate dependency of the dynamic tensile strength of rock," *International Journal of Rock Mechanics and Mining Sciences*, vol. 40, no. 5, pp. 763–777, 2003.
- [22] Q. B. Zhang and J. Zhao, "A review of dynamic experimental techniques and mechanical behaviour of rock materials," *Rock Mechanics and Rock Engineering*, vol. 47, no. 4, pp. 1411–1478, 2014.
- [23] G. Gao, W. Yao, K. Xia, and Z. Li, "Investigation of the rate dependence of fracture propagation in rocks using digital image correlation (DIC) method," *Engineering Fracture Mechanics*, vol. 138, no. 1, pp. 146–155, 2015.
- [24] B. Mahanta, A. Tripathy, V. Vishal, T. N. Singh, and P. G. Ranjith, "Effects of strain rate on fracture toughness and energy release rate of gas shales," *Engineering Geology*, vol. 218, pp. 39–49, 2017.
- [25] M. Mahal, T. Blanksvärd, B. Täljsten, and G. Sas, "Using digital image correlation to evaluate fatigue behavior of strengthened reinforced concrete beams," *Engineering Structures*, vol. 105, pp. 277–288, 2015.
- [26] F. Hild, A. Bouterf, and S. Roux, "Damage measurements via DIC," *International Journal of Fracture*, vol. 191, no. 1–2, pp. 77–105, 2015.
- [27] Ł. Skarżyński and J. Tejchman, "Calculations of fracture process zones on meso-scale in notched concrete beams subjected to three-point bending," *European Journal of Mechanics*, vol. 29, no. 4, pp. 746–760, 2010.
- [28] W. H. Peters and W. F. Ranson, "Digital imaging techniques in experimental stress analysis," *Optical Engineering*, vol. 21, no. 3, pp. 427–431, 1982.
- [29] M. Sutton, W. Wolters, W. Peters, W. Ranson, and S. McNeill, "Determination of displacements using an improved digital correlation method," *Image and Vision Computing*, vol. 1, no. 3, pp. 133–139, 1983.
- [30] C. Zhao, H. Matsuda, C. Morita, and M. R. Shen, "Study on failure characteristic of rock-like materials with an open-hole under uniaxial compression," *Strain*, vol. 47, no. 5, pp. 405–413, 2011.
- [31] C. Zhao, Y. M. Zhou, C. F. Zhao, and C. Bao, "Cracking processes and coalescence modes in rock-like specimens with two parallel pre-existing cracks," *Rock Mechanics and Rock Engineering*, vol. 51, no. 11, pp. 3377–3393, 2018.
- [32] Q. Lin and J. F. Labuz, "Fracture of sandstone characterized by digital image correlation," *International Journal of Rock Mechanics and Mining Sciences*, vol. 60, no. 8, pp. 235–245, 2013.
- [33] H. Zhang, D. H. Fu, H. P. Song et al., "Damage and fracture investigation of three-point bending notched sandstone beams by DIC and AE techniques," *Rock Mechanics and Rock Engineering*, vol. 48, no. 3, pp. 1297–1303, 2015.
- [34] H. H. N. Chen, R. K. L. Su, S. L. Fok, and H. G. Zhang, "Fracture behavior of nuclear graphite under three-point bending tests," *Engineering Fracture Mechanics*, vol. 186, pp. 143–157, 2017.

- [35] M. Bornert, F. ValÃ©s, H. Gharbi, and D. Nguyen Minh, "Multiscale full-field strain measurements for micro-mechanical investigations of the hydromechanical behaviour of clayey rocks," *Strain*, vol. 46, no. 1, pp. 33–46, 2010.
- [36] A. D. Kammers and S. Daly, "Digital image correlation under scanning electron microscopy: methodology and validation," *Experimental Mechanics*, vol. 53, no. 9, pp. 1743–1761, 2013.
- [37] L. L. Wang, M. Bornert, E. Héripré, S. Chanchole, A. Pouya, and B. Halphen, "The mechanisms of deformation and damage of mudstones: a micro-scale study combining ESEM and DIC," *Rock Mechanics and Rock Engineering*, vol. 48, no. 5, pp. 1913–1926, 2015.
- [38] J. P. Zuo, X. S. Wang, and D. Q. Mao, "SEM in-situ study on the effect of offset-notch on basalt cracking behavior under three-point bending load," *Engineering Fracture Mechanics*, vol. 131, pp. 504–513, 2014.
- [39] T. A. Berfield, J. K. Patel, R. G. Shimmin, P. V. Braun, J. Lambros, and N. R. Sottos, "Micro- and nanoscale deformation measurement of surface and internal planes via digital image correlation," *Experimental Mechanics*, vol. 47, no. 1, pp. 51–62, 2007.
- [40] Y. L. Lu, W. S. Li, L. G. Wang et al., "In-situ microscale visualization experiments on microcracking and microdeformation behaviour around a pre-crack tip in a three-point bending sandstone," *International Journal of Rock Mechanics and Mining Sciences*, vol. 114, pp. 175–185, 2019.
- [41] B. Pan, K. M. Qian, H. M. Xie, and A. Asundi, "Topical review: two-dimensional digital image correlation for in-plane displacement and strain measurement: a review," *Measurement Science and Technology*, vol. 20, no. 6, pp. 152–154, 2009.
- [42] D. Lockner, "The role of acoustic emission in the study of rock fracture," *International Journal of Rock Mechanics and Mining Sciences & Geomechanics Abstracts*, vol. 30, no. 7, pp. 883–899, 1993.
- [43] C. D. Martin and N. A. Chandler, "The progressive fracture of Lac du Bonnet granite," *International Journal of Rock Mechanics and Mining Sciences & Geomechanics Abstracts*, vol. 31, no. 6, pp. 643–659, 1994.
- [44] E. Eberhardt, D. Stead, B. Stimpson, and R. S. Read, "Identifying crack initiation and propagation thresholds in brittle rock," *Canadian Geotechnical Journal*, vol. 35, no. 2, pp. 222–233, 1998.
- [45] A. L. Rosa, R. C. Yu, G. Ruiz, L. Saucedo, and J. L. A. O. Sousa, "A loading rate dependent cohesive model for concrete fracture," *Engineering Fracture Mechanics*, vol. 82, pp. 195–208, 2012.
- [46] G. Ruiz, X. X. Zhang, R. C. Yu, R. Porras, E. Poveda, and J. R. del Viso, "Effect of loading rate on fracture energy of high-strength concrete," *Strain*, vol. 47, no. 6, pp. 518–524, 2011.

